

Magnetic Reconnection as an Erosion Mechanism for Magnetic Switchbacks

G.H.H. Suen^{1,*}, C.J. Owen¹, D. Verscharen¹, T.S. Horbury², P. Louarn³, and R. De Marco⁴

¹ Mullard Space Science Laboratory, University College London, Holmbury St. Mary, Dorking, Surrey RH5 6NT, UK

² Imperial College London, South Kensington Campus, London SW7 2AZ, UK

³ Institut de Recherche en Astrophysique et Planétologie, 9 avenue du Colonel Roche, 31028 Toulouse Cedex 4, France

⁴ INAF – Istituto di Astrofisica e Planetologia Spaziali, Via Fosso del Cavaliere 100, 00133, Roma, Italy

Received ; accepted

ABSTRACT

Context. Magnetic switchbacks are localised polarity reversals in the radial component of the heliospheric magnetic field. Observations from *Parker Solar Probe* (PSP) have shown that they are a prevalent feature of the near-Sun solar wind. However, observations of switchbacks at 1 au and beyond are less frequent, suggesting that these structures evolve and potentially erode through yet-to-be identified mechanisms as they propagate away from the Sun.

Aims. We search for magnetic switchbacks undergoing magnetic reconnection, characterise them, and then evaluate the viability of reconnection as a possible channel for their erosion.

Methods. We analyse magnetic field and plasma data from the Magnetometer and Solar Wind Analyser instruments aboard *Solar Orbiter* between 10 August and 30 August 2021. During this period, the spacecraft was 0.6 – 0.7 au from the Sun. Using hodographs and Walén analysis methods, we test for rotational discontinuities (RDs) in the magnetic field and reconnection-associated outflows at the boundaries of the identified switchback structures.

Results. We identify three instances of reconnection occurring at the trailing edge of magnetic switchbacks, with properties consistent with existing models describing reconnection in the solar wind. Based on these observations, we propose a scenario through which reconnection can erode a switchback and we estimate the timescales over which this occurs. For our events, the erosion timescales are much shorter than the expansion timescale and thus, the complete erosion of all three observed switchbacks would occur well before they reach 1 au. Furthermore, we find that the spatial scale of these switchbacks would be considerably larger than is typically observed in the inner heliosphere if the onset of reconnection occurs close to the Sun. Hence, our results suggest that the onset of reconnection must occur during transport in the solar wind in our cases. These results suggest that reconnection can contribute to the erosion of switchbacks and may explain the relative rarity of switchback observations at 1 au.

Key words. Sun: solar wind – Sun: heliosphere – plasmas – magnetic reconnection

1. Introduction

Magnetic reconnection is a fundamental energy conversion process occurring in many laboratory and astrophysical plasmas. Reconnection converts magnetic energy into kinetic and thermal energy through a change in magnetic field topology across current sheets (Pontin 2011; Gosling 2012; Cassak 2016; Hesse & Cassak 2020). In the context of heliospheric physics, reconnection is a key candidate process to explain coronal heating (Parker 1983, 1988) and solar wind acceleration (Zank et al. 2014; Khabarova et al. 2015; Adhikari et al. 2019).

Statistical studies show that up to 20% of the magnetic energy is converted into particle heating, while the remainder is converted into particle acceleration, creating a pair of oppositely directed bulk outflow jets that stream into the background plasma (Enžl et al. 2014; Mistry et al. 2017). The proportion of magnetic energy converted into particle heating and acceleration depends on the magnetic shear angle (Drake et al. 2009). In the rest frame of the reconnection current sheet (RCS), the bulk velocity of the outflow jets is of the order of the local Alfvén speed, although reconnection events with sub-Alfvénic outflows are not unusual (Haggerty et al. 2018; Phan et al. 2020).

The reconnection model described by Gosling et al. (2005a) is frequently used to interpret the spatial structure of reconnection outflows in the solar wind. The RCS bifurcates, forming a pair of standing Alfvénic rotational discontinuities (RDs) in the magnetic field at the edges of the outflow region. According to the Rankine-Hugoniot conditions, the RDs must be Alfvénic in nature (Hudson 1970). The outflow region has weaker magnetic field strength and increased plasma temperature and density compared to the background plasma. Interplanetary coronal mass ejections (ICMEs) (McComas et al. 1994; Gosling et al. 2005a), the heliospheric current sheet (HCS) (Gosling et al. 2005b, 2006b; Phan et al. 2021), and the regular solar wind (Gosling et al. 2007; Phan et al. 2020) are locations where reconnection occurs.

Magnetic switchbacks are localised polarity reversals in the radial component of the heliospheric magnetic field (HMF) (Bale et al. 2019; Dudok de Wit et al. 2020; Krasnoselskikh et al. 2020). They are often associated with increases in the radial component of the bulk proton velocity by a significant fraction of the local Alfvén speed (Matteini et al. 2014; Horbury et al. 2018; Kasper et al. 2019; Horbury et al. 2020b). Measurements of suprathermal electrons help us determine the magnetic connectivity during switchback encounters. These electrons stream

* e-mail: ho.suen.20@ucl.ac.uk

away from the Sun along the open HMF, forming a field-aligned beam known as the strahl (Owens & Forsyth 2013). The presence and pitch angle of this beam can be an indicator of the connectivity of open field lines to the Sun (Feldman et al. 1975; Rosenbauer et al. 1977): assuming the direction of the strahl velocity indicates the anti-sunward direction along the encountered magnetic field line, the strahl pitch angle in the reversed section of a folded field configuration, such as switchbacks, is the same as in the surrounding HMF (Kasper et al. 2019).

Switchbacks have previously been observed by *Helios* (Horbury et al. 2018), *Ulysses* (Balogh et al. 1999), and *ACE* (Owens et al. 2013) at heliocentric distances between 0.3 – 2.4 au, both near the ecliptic plane and at high heliolatitudes. Recent observations from *Parker Solar Probe* (PSP) show that switchbacks are a prevalent feature of the near-Sun solar wind (Bale et al. 2019; Kasper et al. 2019), present for roughly 75% of the time during PSP Encounter 1 (Horbury et al. 2020b). These structures are convected over the observing spacecraft on timescales ranging from a few minutes to a few hours (Dudok de Wit et al. 2020), and have transverse scales comparable to solar granulation and supergranulation (Fargette et al. 2021).

The mechanisms responsible for the formation of switchbacks are still under debate. Recent studies suggest that at least some proportion of the total switchback population originates from the solar corona (de Pablos et al. 2022; Telloni et al. 2022). Processes linked to interchange reconnection (Fisk & Kasper 2020; Drake et al. 2021) and coronal jets (Sterling & Moore 2020; Neugebauer & Sterling 2021) are invoked to explain the formation of these structures in the corona. Other studies suggest that switchback formation can occur locally in the solar wind: for example, based on PSP observations, Schwadron & McComas (2021) propose a mechanism through which switchbacks are generated by velocity shears between fast and slow solar wind streams. MHD simulations suggest that Alfvén wave steepening (Squire et al. 2020; Johnston et al. 2022; Squire et al. 2022) and Kelvin-Helmholtz instabilities (Ruffolo et al. 2020; Kieokaew et al. 2021) are viable formation mechanisms.

At heliocentric distances of 1 au and beyond, switchbacks are less frequently seen than in the inner heliosphere, suggesting that these structures evolve and eventually erode as they propagate away from the Sun (Tenerani et al. 2020, 2021). Magnetic reconnection is one possible mechanism that can enhance erosion of a switchback by removing magnetic flux from the polarity-reversed section of the magnetic field. Observations from *Helios* (Gosling et al. 2006a) and PSP (Froment et al. 2021) show that reconnection may occur at switchback boundaries.

We present examples of switchback boundary reconnection events observed by *Solar Orbiter* and use them to evaluate the effectiveness of magnetic reconnection as an erosion mechanism for switchbacks. In Section 2, we describe our data and analysis methods. In Section 3, we show observations of three instances of switchback reconnection. In Section 4, we present our interpretation of the switchback and reconnection geometry based on the observations, and estimate the remaining lifetime of the switchbacks. In Section 5, we summarise our findings and discuss their implications on the global properties of switchbacks in the solar wind.

2. Data and Methods

2.1. Instrumentation

We use publicly available magnetic field and plasma data from the Magnetometer (MAG, Horbury et al. 2020a) and Solar Wind

Analyser (SWA, Owen et al. 2020) instruments on board *Solar Orbiter*. MAG consists of a pair of fluxgate magnetometers mounted on the spacecraft boom and has a measurement cadence of 8 vectors/second in normal mode operation during this period. SWA is comprised of three sensors — of particular relevance to this study are the SWA-Proton Alpha Sensor (SWA-PAS) and SWA-Electron Analyser System (SWA-EAS). SWA-PAS delivers ground-calculated proton moments (velocity, temperature, and density) once every 4 seconds for periods of normal mode operation. We use electron strahl pitch angle distribution (PAD) data at > 70 eV from SWA-EAS, when available, at a cadence of 1 measurement per 100 seconds.

For this case study, we sample a time interval during August 2021 for magnetic reconnection outflows in the solar wind, when the spacecraft was at a heliocentric distance of 0.6 – 0.7 au. We exclude outflows with crossing durations less than 20 seconds to ensure that there are at least five proton measurements inside the outflow region. Out of the ten events that satisfy the selection criteria, three are associated with potential magnetic switchbacks.

2.2. Reference Frames

The MAG and SWA data are initially provided in the RTN coordinate system. This is a spacecraft-centred reference frame in which $\hat{\mathbf{R}}$ is the Sun-spacecraft radial vector, $\hat{\mathbf{T}}$ is the cross product between the Sun’s rotation axis and $\hat{\mathbf{R}}$, and $\hat{\mathbf{N}}$ completes the triad.

We rotate vector quantities into a current sheet-aligned (lmn)-frame, defined by the basis vectors $\hat{\mathbf{l}}$, $\hat{\mathbf{m}}$, and $\hat{\mathbf{n}}$. This coordinate system is derived using the hybrid minimum variance analysis (MVAB) method (Gosling & Phan 2013). We calculate the current sheet normal direction $\hat{\mathbf{n}}$ as:

$$\hat{\mathbf{n}} = \frac{\mathbf{B}_1 \times \mathbf{B}_2}{|\mathbf{B}_1 \times \mathbf{B}_2|}, \quad (1)$$

where \mathbf{B}_1 and \mathbf{B}_2 are the instantaneous magnetic field vectors on either side of the current sheet. $\hat{\mathbf{m}}$ is given by $\hat{\mathbf{m}} = \hat{\mathbf{l}} \times \hat{\mathbf{n}}$, where $\hat{\mathbf{l}}$ is the maximum variance direction unit vector derived from the standard MVAB method developed by Sonnerup & Cahill (1967). $\hat{\mathbf{l}}$ completes the triad as $\hat{\mathbf{l}} = \hat{\mathbf{m}} \times \hat{\mathbf{n}}$. Since the MVAB method requires the solution of an eigenvalue problem, the reliability of $\hat{\mathbf{l}}$ (and hence, $\hat{\mathbf{m}}$) depends on non-degeneracy in the eigenvalues corresponding to the maximum (λ_1) and intermediate (λ_2) variance direction eigenvectors. Typically, this non-degeneracy condition is satisfied if $\lambda_1/\lambda_2 \geq 10$ (Sonnerup & Scheible 1998). Assuming the current sheet is planar and $B_n \ll B_m$, we expect $\hat{\mathbf{l}}$, $\hat{\mathbf{m}}$, and $\hat{\mathbf{n}}$ to broadly correspond to the exhaust outflow direction, the x-line direction and current sheet normal direction, respectively.

The deHoffman-Teller (HT) frame is defined as the reference frame in which the convection electric field vanishes (de Hoffmann & Teller 1950). We find the RTN HT frame velocity \mathbf{v}_{HT} by solving the linear matrix equation (Paschmann & Sonnerup 2008) over a given measurement interval

$$\begin{pmatrix} \langle B_T^2 + B_N^2 \rangle & \langle -B_R B_T \rangle & \langle -B_R B_N \rangle \\ \langle -B_R B_T \rangle & \langle B_R^2 + B_N^2 \rangle & \langle -B_T B_N \rangle \\ \langle -B_R B_N \rangle & \langle -B_T B_N \rangle & \langle B_R^2 + B_T^2 \rangle \end{pmatrix} \begin{pmatrix} v_{HT,R} \\ v_{HT,T} \\ v_{HT,N} \end{pmatrix} = \begin{pmatrix} \langle E_T B_N - E_N B_T \rangle \\ \langle E_N B_R - E_R B_N \rangle \\ \langle E_R B_T - E_T B_R \rangle \end{pmatrix}, \quad (2)$$

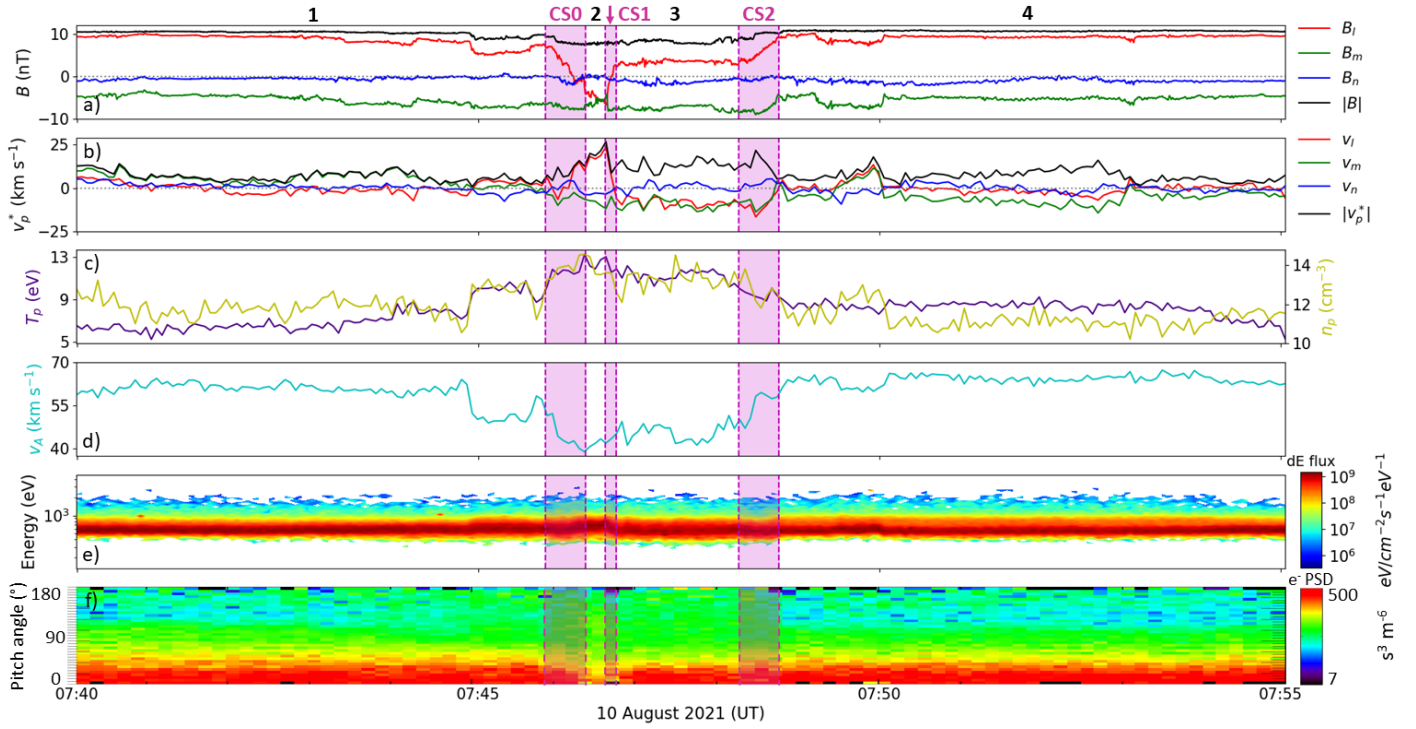


Fig. 1. Combined magnetic field, proton, and electron strahl PAD time series data for Event 1 in the hybrid MVAB lmn -frame. a) Magnetic field vector with the magnetic field strength in black. b) Proton bulk velocity with the proton bulk speed in black. The average proton bulk velocity $\langle \mathbf{v}_p \rangle$ over this interval has been removed. In both panels, the l -component is in red, the m -component is in green, and the n -component is in blue. c) Proton temperature (left scale, purple) and number density (right scale, gold). d) Alfvén speed v_A . e) 1D proton energy spectrogram. f) Electron strahl PAD for energies > 70 eV. The dashed lines mark the region boundaries identified in the text and numbered at the top of the figure.

where \mathbf{B} is the magnetic field vector, \mathbf{E} is the convection electric field, and the angled brackets $\langle \rangle$ denote averages over the measurements used in this calculation. In the ideal MHD limit, we assume that $\mathbf{E} = -\mathbf{v}_p \times \mathbf{B}$ where \mathbf{v}_p is the RTN frame bulk plasma velocity.

2.3. Testing for Rotational Discontinuities

Magnetic hodographs are used to illustrate the spatial and temporal evolution of \mathbf{B} in 3D; they are plotted in pairs for the lm and ln -planes of the lmn -frame (Sonnerup & Scheible 1998). If an RD is present across the current sheet, we expect to see the temporal variation of \mathbf{B} trace a semi-circular arc in the lm -plane hodograph and a vertical line at $B_n \neq 0$ in the ln -plane hodograph.

We use hodographs in conjunction with the Walén relation to test for Alfvénic RDs across current sheets (Khrabrov & Sonnerup 1998):

$$\mathbf{v}'_p = \pm \mathbf{v}_A = \pm \frac{\mathbf{B}}{\sqrt{\mu_0 \rho}}, \quad (3)$$

where $\mathbf{v}'_p = \mathbf{v}_p - \mathbf{v}_{HT}$ is the HT frame bulk plasma velocity, μ_0 is the permeability of free space, and ρ is the plasma mass density. The sign in Eq. 3 indicates whether the Alfvénic fluctuations in \mathbf{v}'_p and \mathbf{B} are correlated (positive) or anti-correlated (negative). We test the strength of the Walén relation using component-by-component scatter plots of \mathbf{v}'_p against \mathbf{v}_A , using the least-squares linear regression method to determine the line of best fit. From Equation 3, a line of best fit slope of ± 1 in the Walén plot is an indicator of an ideal Alfvénic RD, although previous works suggest that slopes with magnitudes between 0.5 – 1 are suf-

ficient to demonstrate the existence of an RD across a current sheet (Paschmann et al. 2005; Dong et al. 2017).

3. Results

3.1. Event 1 – 10 August 2021 07:45:50 - 07:48:45 UT

Figure 1 provides a general overview of the magnetic field and solar wind conditions observed between 07:40:00 and 07:55:00 UT on 10 August 2021, recorded at a heliocentric distance of 0.72 au. Panel a) shows the magnetic field \mathbf{B} and b) shows the proton bulk velocity \mathbf{v}_p^* in the lmn -frame. In both panels, the l -component is in red, the m -component is in green, and the n -component is in blue. Panel c) shows the proton temperature T_p in purple and proton number density n_p in gold, d) shows the Alfvén speed v_A , e) shows the 1D proton energy spectrogram, and f) shows the electron strahl PAD for energies > 70 eV. We remove the average proton bulk velocity $\langle \mathbf{v}_p \rangle$ across this interval from the data, such that $\mathbf{v}_p^* = \mathbf{v}_p - \langle \mathbf{v}_p \rangle$.

Table 1. Event 1 lmn -frame basis vectors for CS0 and CS1 + CS2 expressed in RTN coordinates.

Current sheet	lmn -frame basis vectors (R, T, N)
CS0	$\hat{\mathbf{i}} = (0.660, -0.216, 0.719)$ $\hat{\mathbf{m}} = (0.016, -0.954, -0.300)$ $\hat{\mathbf{n}} = (0.751, 0.210, -0.626)$
CS1 + CS2	$\hat{\mathbf{i}} = (0.677, -0.343, 0.651)$ $\hat{\mathbf{m}} = (0.086, 0.916, 0.393)$ $\hat{\mathbf{n}} = (-0.731, -0.210, 0.649)$

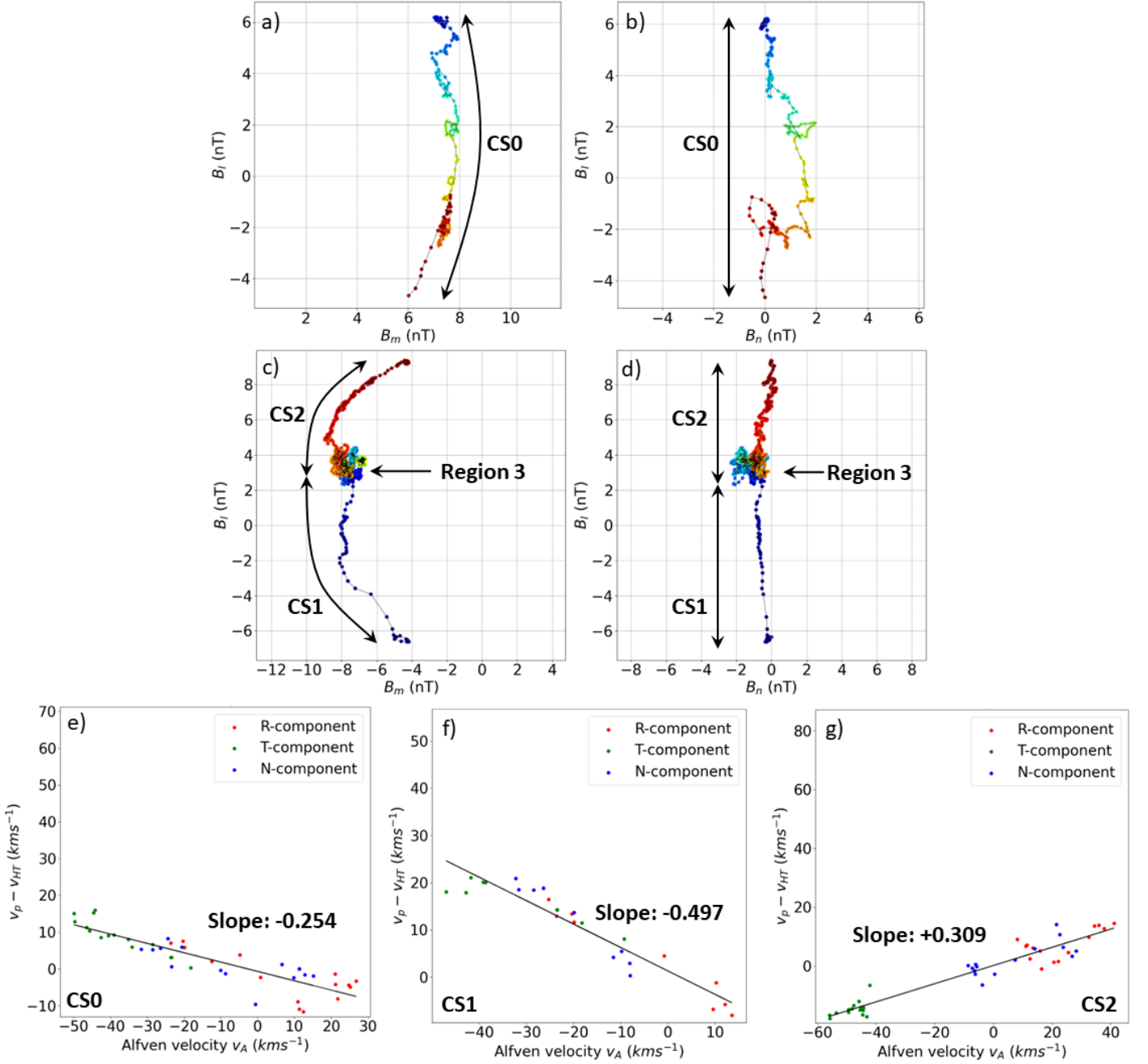


Fig. 2. Magnetic hodographs and Walén plots for CS0 (07:45:50 – 07:46:20 UT), CS1 (07:46:35 – 07:46:43 UT), and CS2 (07:48:15 – 07:48:45 UT) in Event 1. Time progression in the hodographs is represented by the colour of the dots, with earlier times in blue and later times in red. The red, green, and blue dots in the Walén plots represent the R , T , and N -components of the Alfvén velocity \mathbf{v}_A and the HT frame bulk plasma velocity $\mathbf{v}_p - \mathbf{v}_{HT}$. a) lm -plane hodograph for CS0. b) ln -plane hodograph for CS0. c) lm -plane hodograph for CS1 and CS2. d) ln -plane hodograph for CS1 and CS2. e) Walén plot for CS0. f) Walén plot for CS1. g) Walén plot for CS2.

In RTN coordinates, $\langle \mathbf{v}_p \rangle = (322.2, -5.6, -5.6)_{RTN} \text{ km s}^{-1}$ across this time interval and the predominant HMF polarity is in the anti-sunward (+ R) direction. We divide this interval into several regions marked by the vertical dashed lines. Regions 1 (07:40:00 – 07:45:50 UT) and 4 (07:48:45 – 07:55:00 UT) correspond to the period of quiet HMF and steady, slow solar wind surrounding this event. The regions shaded in purple are centered around sharp discontinuities in the magnetic field that we identify as current sheets.

We derive the lmn -frames for the current sheets at the leading (CS0) and trailing edges (CS1, CS2) of this event using the hybrid MVAB method. As the trailing edge current sheets are bi-

furcated, we perform the MVAB analysis from the start of CS1 to the end of CS2. Table 1 shows the lmn -frame basis vectors for these current sheets. The angular differences between the corresponding basis vector pairs of both frames are small, ranging from 1.7° to 8.3° . Thus, the lmn -frames for the leading and trailing edges of this event are roughly aligned. As we are interested in the properties of the reconnection outflow, we visualise its properties in the lmn -frame of the trailing edge current sheet in Figures 1a and 1b. We do the same for the overview plots of the other two events.

Across CS0 (07:45:50 – 07:46:20 UT), the polarity of the radial component of the HMF, B_R , flips from the anti-sunward di-

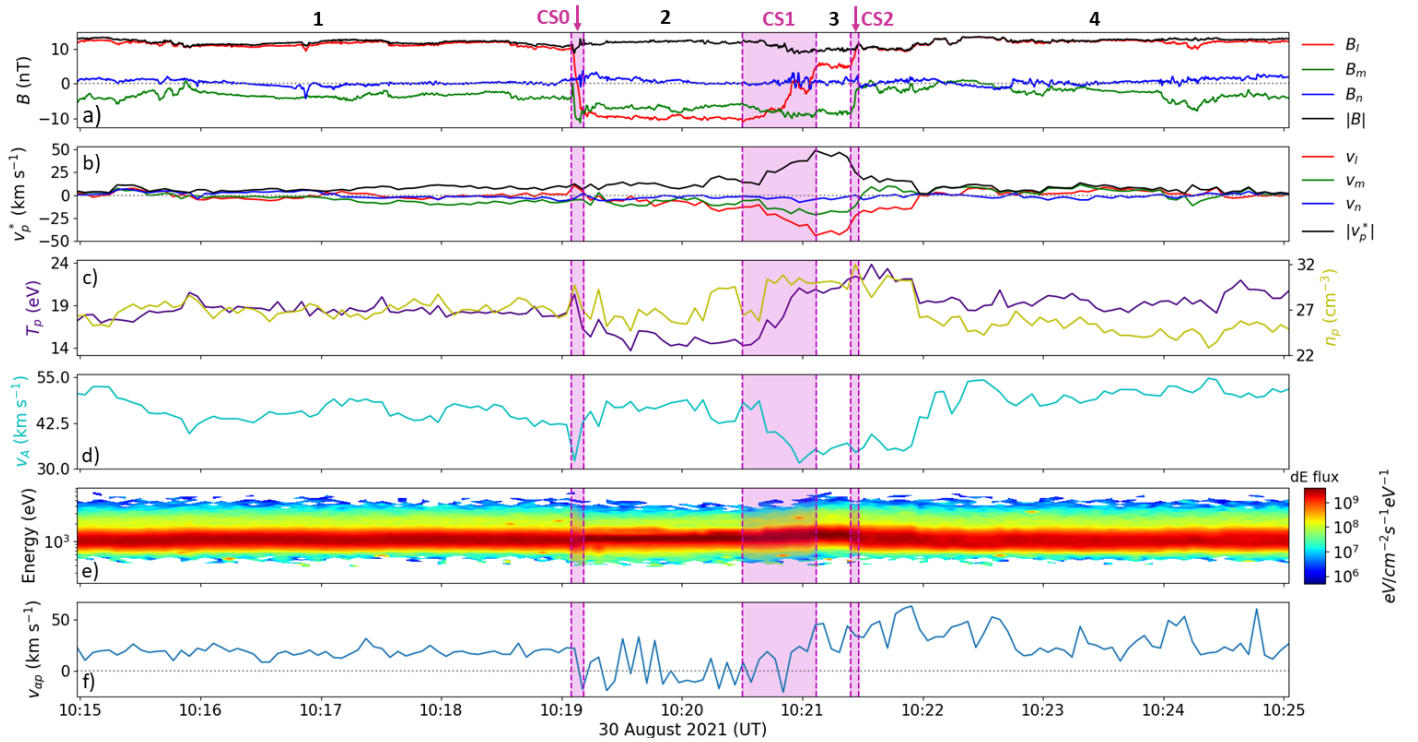


Fig. 3. Combined magnetic field and proton time series data for Event 2 in the hybrid MVAB lmn -frame. The figure layout is the same as in Figure 1 except for the absence of electron strahl PAD data, which are unavailable for this interval. Panel f) instead shows the signed magnitude of the alpha-proton velocity difference vector v_{ap} .

reconnection to the sunward direction. In the lmn -frame of this event, this corresponds to a reversal in the B_l component of the magnetic field from +7 nT to -4 nT. Due to the relatively strong B_m component, the maximum magnetic shear angle across this current sheet is 77.2° . There is a 20% decrease in the average magnetic field strength $|\mathbf{B}|$, from 10 nT in Region 1 to 8 nT in CS0. v_l , the l -component of \mathbf{v}_p^* , increases from 0 km s $^{-1}$ to +10 km s $^{-1}$, and the average proton bulk speed $|\mathbf{v}_p^*|$ increases from 4 km s $^{-1}$ to 13 km s $^{-1}$. Here, we also measure the maximum T_p of 13 eV and n_p of 14 cm $^{-3}$.

Region 2 (07:46:20 – 07:46:35 UT) encompasses the polarity-reversed section of this event. B_l decreases to -6 nT, v_l increases further to +24 km s $^{-1}$ and $|\mathbf{v}_p^*|$ increases to +27 km s $^{-1}$. This is roughly 68% of the local v_A of 40 km s $^{-1}$. There is minimal change in $|\mathbf{B}|$, T_p , and n_p in this region compared to CS0. The electron strahl PAD peaks in the field-aligned direction (0°) both in the background HMF and in the regions containing polarity-reversed magnetic flux (CS0 and Region 2).

Across CS1 (07:46:35 – 07:46:43 UT) and CS2 (07:48:15 – 07:48:45 UT), the HMF polarity reverts back towards the anti-sunward direction observed in Region 1. B_l increases from -6 nT to +3 nT across CS1 and then increases again from +3 nT to +9 nT across CS2. In Region 3 (07:46:43 – 07:48:15 UT), B_l remains roughly constant at +4 nT; this is intermediate between its value in Region 2 and the background HMF in Regions 1 and 4. The total magnetic shear angle across CS1, CS2, and Region 3 is 117° . There is a slight decrease in $|\mathbf{v}_p^*|$ from 25 km s $^{-1}$ to an average of 15 km s $^{-1}$. v_l sharply decreases across CS1 and is negative in Region 3, with an average value of -10 km s $^{-1}$. We observe gradual decreases in T_p from 12.5 eV to 9 eV and in n_p from 14 cm $^{-3}$ to 12 cm $^{-3}$. Moreover, we note a brief strahl dropout across CS1 and the latter part of Region 2, accompanied

by a sustained broadening of the strahl PAD in CS1 and Region 3. As both features are also present in the raw electron counts data, they are unlikely to be aliasing effects caused by the rapid rotation of the magnetic field.

Using the methods described in Section 2.3, Figure 2 shows the magnetic hodographs and Walén plots for CS0, CS1, and CS2. Panels a) and b) show the hodographs for CS0 in its associated lmn -frame, panels c) and d) show the hodographs for CS1 and CS2 combined in their associated lmn -frame, and panels e) – g) show the Walén plots for CS0, CS1, and CS2. For the Walén plots, we re-sample \mathbf{B} on \mathbf{v}_p as MAG has higher time resolution than PAS. We also include all data points 15 seconds before and after the current sheet crossing in the analysis. This ensures that a representative number of data points are included in the Walén plots, even for short-duration current sheets containing only a single proton measurement inside the current sheet. The choice of 15 seconds is deliberate, to prevent data points from CS1 contaminating the analysis for CS0 and vice-versa. For consistency, we apply the same method and the same timeframe of 15 seconds to all three events.

In the lm -plane hodographs (Figure 2a, 2c), \mathbf{B} across all three current sheets traces an arc consistent with the measured magnetic shear angle. In the ln -plane hodograph for CS0 (Figure 2b), $B_n \approx 0$ nT at the start and end of the interval, but deflects out to $B_n \approx +2$ nT in the middle. For CS1 and CS2 (Figure 2d), \mathbf{B} has a small B_n component of -1.0 nT and traces a quasi-vertical line in the ln -plane. In Figures 2c and 2d, the rotation of \mathbf{B} is split into two arcs that individually correspond to CS1 and CS2. They are separated by an interval where the orientation of \mathbf{B} does not change significantly, corresponding to Region 3. The magnitudes of the gradient of the line of best fit of the Walén plots for CS0 (-0.254), CS1 (-0.497), and CS2 (+0.309) fall below the range 0.5 – 1 expected for an Alfvénic structure.

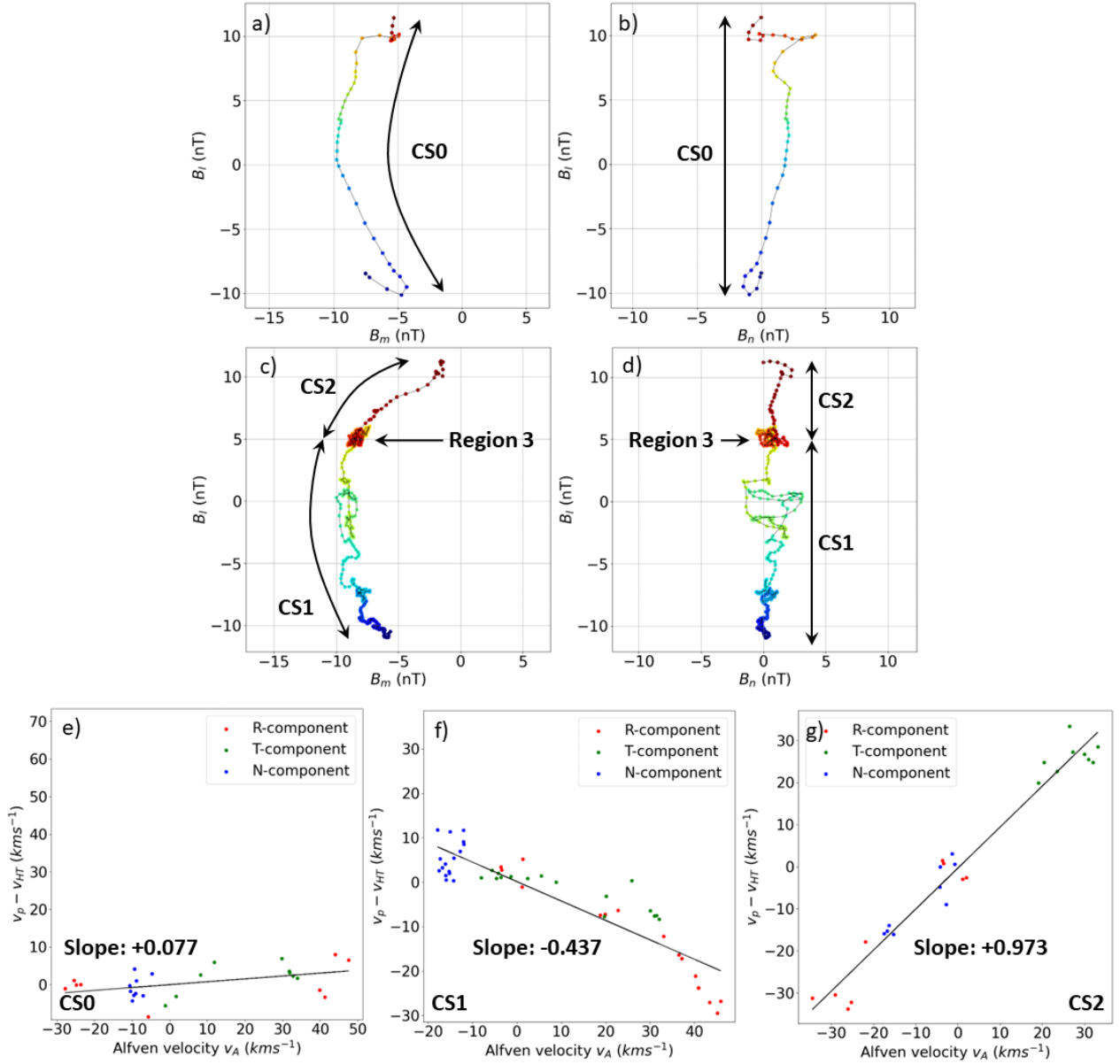


Fig. 4. Magnetic hodographs and Walén plots for CS0 (10:19:05 – 10:19:11 UT), CS1 (10:20:50 – 10:21:07 UT), and CS2 (10:21:24 – 10:21:28 UT) in Event 2. The figure layout is the same as in Figure 2.

3.2. Event 2 - 30 August 2021 10:19:05 - 10:21:28 UT

Figure 3 shows Event 2 observed between 10:15:00 and 10:25:00 UT on 30 August 2021 at a heliocentric distance of 0.61 au. The figure layout is the same as in Figure 1, except for the absence of electron strahl PAD data. In lieu of the strahl PAD, panel f) instead shows the signed magnitude of the alpha-proton velocity difference vector $v_{\alpha p} = |\mathbf{v}_{\alpha} - \mathbf{v}_{p}| \cdot \text{sgn}(v_{\alpha,R} - v_{p,R})$, which we use as an alternative method of checking for folded field configurations (Fedorov et al. 2021). We obtain this data using the techniques described in De Marco et al. (2023). For this interval, $\langle \mathbf{v}_{p} \rangle = (438.8, -14.6, -2.3)_{RTN} \text{ km s}^{-1}$ and the predominant HMF polarity before (Region 1, 10:15:00 – 10:19:05 UT) and after (Region 4, 10:21:28 – 10:25:00 UT) this event is in the sunward direction.

We again identify three regions of strong magnetic gradients and label them CS0, CS1, and CS2. Table 2 shows the lmn -frame basis vectors for these current sheets. The angular differences

between the basis vectors of the lmn -frames for CS0 and CS1 + CS2 are 21.6° for $\hat{\mathbf{l}}$, 28.4° for $\hat{\mathbf{m}}$, and 18.9° for $\hat{\mathbf{n}}$.

Table 2. Event 2 lmn -frame basis vectors for CS0 and CS1 + CS2 expressed in RTN coordinates.

Current sheet	lmn -frame basis vectors (R, T, N)
CS0	$\hat{\mathbf{l}} = (0.971, -0.220, -0.093)$ $\hat{\mathbf{m}} = (-0.185, -0.939, 0.287)$ $\hat{\mathbf{n}} = (-0.151, -0.261, -0.953)$
CS1 + CS2	$\hat{\mathbf{l}} = (-0.835, 0.550, -0.020)$ $\hat{\mathbf{m}} = (-0.452, -0.665, 0.594)$ $\hat{\mathbf{n}} = (0.313, 0.505, 0.804)$

B_R flips from its sunward-orientation in Region 1 to an anti-sunward orientation in Region 2 (10:19:11 – 10:20:30 UT) across CS0 (10:19:05 – 10:19:11 UT). In the lmn -frame, this is

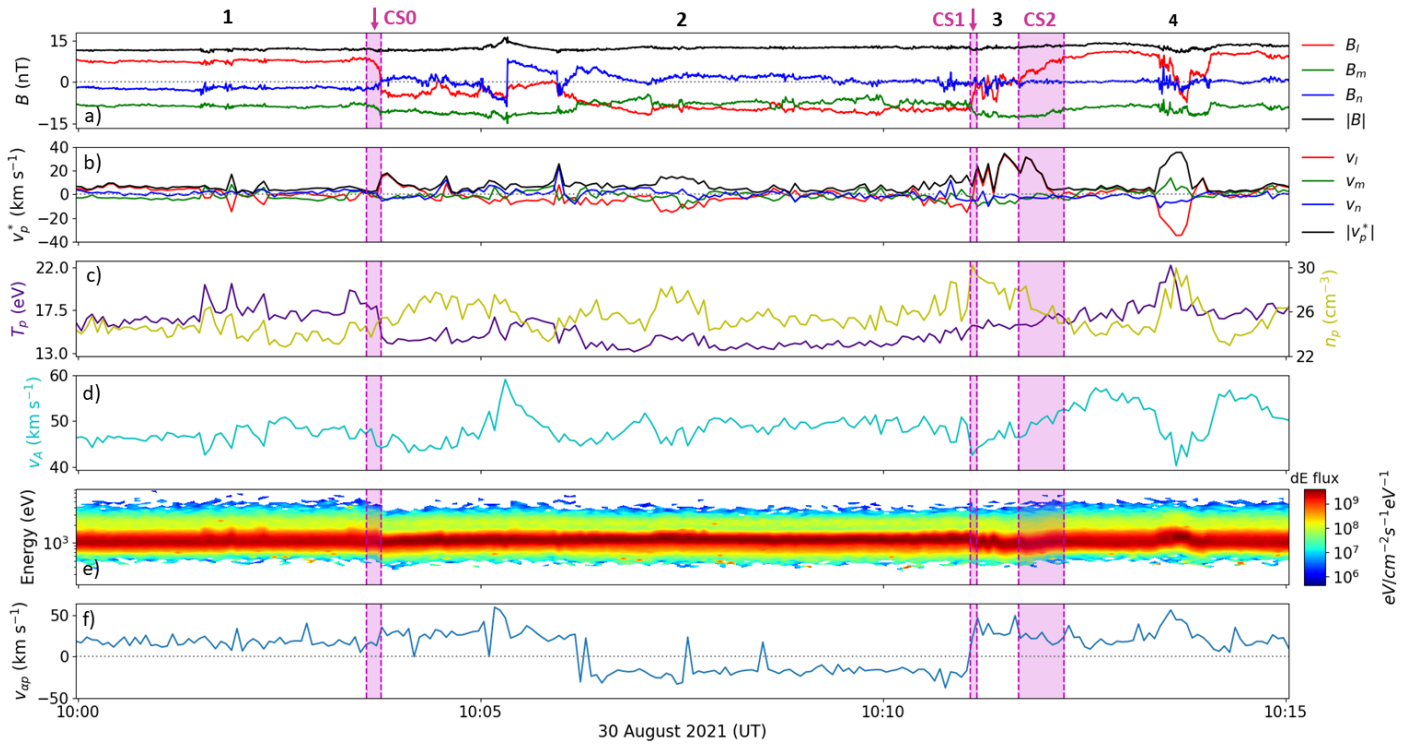


Fig. 5. Combined magnetic field and proton time series data for Event 3 in the hybrid MVAB lmn -frame. The figure layout is the same as Figure 3.

visible as a reversal in B_l from +10 nT to -9 nT; the maximum magnetic shear angle across this current sheet is 113° . There are no major changes in $|\mathbf{B}|$, v_l , and $|\mathbf{v}_p^*|$ in this region for their values in the background HMF in Region 1. T_p decreases from 19 eV to 14 eV and there is a brief spike in n_p up to a value of 29 cm^{-3} .

Region 2 corresponds to the polarity-reversed section of this event. B_l and $|\mathbf{B}|$ both remain approximately constant at -10 nT and 12 nT, respectively. v_l decreases gradually over Region 2 from 0 km s^{-1} to -14 km s^{-1} , while there is a very slight increase in $|\mathbf{v}_p^*|$ from 7 km s^{-1} to 14 km s^{-1} . This is around 30% of the average local $v_A \sim 45 \text{ km s}^{-1}$. We measure a roughly constant average T_p of 14 eV and fluctuations in n_p about an average value of 25 cm^{-3} .

B_l reverses from -10 nT to +10 nT in two steps across CS1 (10:20:30 – 10:21:07 UT) and CS2 (10:21:24 – 10:21:28 UT), dwelling at +5 nT in Region 3 (10:21:07 – 10:21:24 UT). The total magnetic shear across CS1 and CS2 is 134° and $|\mathbf{B}|$ decreases from 12.5 nT to 10 nT. Across CS1, v_l continues decreasing at a faster rate than in Region 2, reaching a minimum value of -45 km s^{-1} in Region 3. $|\mathbf{v}_p^*|$ peaks at 50 km s^{-1} , a value $\sim 43\%$ greater than the local $v_A \sim 35 \text{ km s}^{-1}$. We observe increases in T_p from 14 eV to 25 eV and n_p from 25 cm^{-3} to 30 cm^{-3} .

Figure 4 shows the hodographs and Walén plots for Event 2, the format of this figure is the same as in Figure 2. The arc traced by \mathbf{B} in the lmn -frame for CS0, CS1, and CS2 is consistent with the measured magnetic shear. Across the trailing edge current sheets, the largest rotation in \mathbf{B} occurs over CS1. In the ln -plane, \mathbf{B} traces an approximately vertical line and has a B_n component of +0.5 nT. Around 10:21:00, there are fluctuations in B_n of $\pm 2.5 \text{ nT}$ inside CS1. The Walén plot gradients of +0.077 for CS0 and -0.437 for CS1 are below the range expected for an Alfvénic RD. Conversely, the Walén plot gradient of +0.973 for CS2 indicates that the discontinuity in \mathbf{B} across this structure is Alfvénic.

3.3. Event 3 - 30 August 2021 10:03:46 - 10:12:15 UT

Event 3 (Figure 5) is observed between 10:00:00 UT to 10:15:00 UT on 30 August when *Solar Orbiter* was at a heliocentric distance of 0.61 au. This event has a duration of around eight minutes, four times greater than that of Events 1 and 2. Event 3 occurs in close temporal proximity to Event 2, thus $\langle \mathbf{v}_p \rangle$ and the background HMF polarity for both events are similar. Table 3 shows the lmn -frame basis vectors for CS0 and CS1 + CS2. The angular differences between the basis vectors of these lmn -frames are 24.6° for $\hat{\mathbf{l}}$, 20.2° for $\hat{\mathbf{m}}$, and 13.9° for $\hat{\mathbf{n}}$.

Table 3. Event 3 lmn -frame basis vectors for CS0 and CS1 + CS2 expressed in RTN coordinates.

Current sheet	lmn -frame basis vectors (R, T, N)
CS0	$\hat{\mathbf{l}} = (-0.970, -0.240, 0.037)$
	$\hat{\mathbf{m}} = (-0.235, 0.889, -0.394)$
	$\hat{\mathbf{n}} = (0.061, -0.391, -0.918)$
CS1 + CS2	$\hat{\mathbf{l}} = (-0.977, 0.177, 0.120)$
	$\hat{\mathbf{m}} = (-0.115, -0.908, 0.403)$
	$\hat{\mathbf{n}} = (0.180, 0.308, 0.907)$

B_R in Region 2 (10:03:46 – 10:11:05 UT) is in the anti-sunward direction, opposite to the polarity of the background HMF in Regions 1 (10:00:00 – 10:03:35 UT) and 4 (10:12:15 – 10:15:00 UT). This polarity reversal occurs across CS0 (10:03:35 – 10:03:46 UT), where B_l reverses from +8 nT to -4 nT with a magnetic shear angle of 61° . $|\mathbf{B}|$, v_l , and $|\mathbf{v}_p^*|$ do not deviate noticeably from their values in Region 1. T_p decreases from 17 eV to 14 eV while there is a slight increase in n_p from 23.5 cm^{-3} to 25.5 cm^{-3} .

From 10:03:46 – 10:05:20, B_l remains roughly constant at -5 nT and decreases further to -10 nT from 10:05:55 UT onwards.

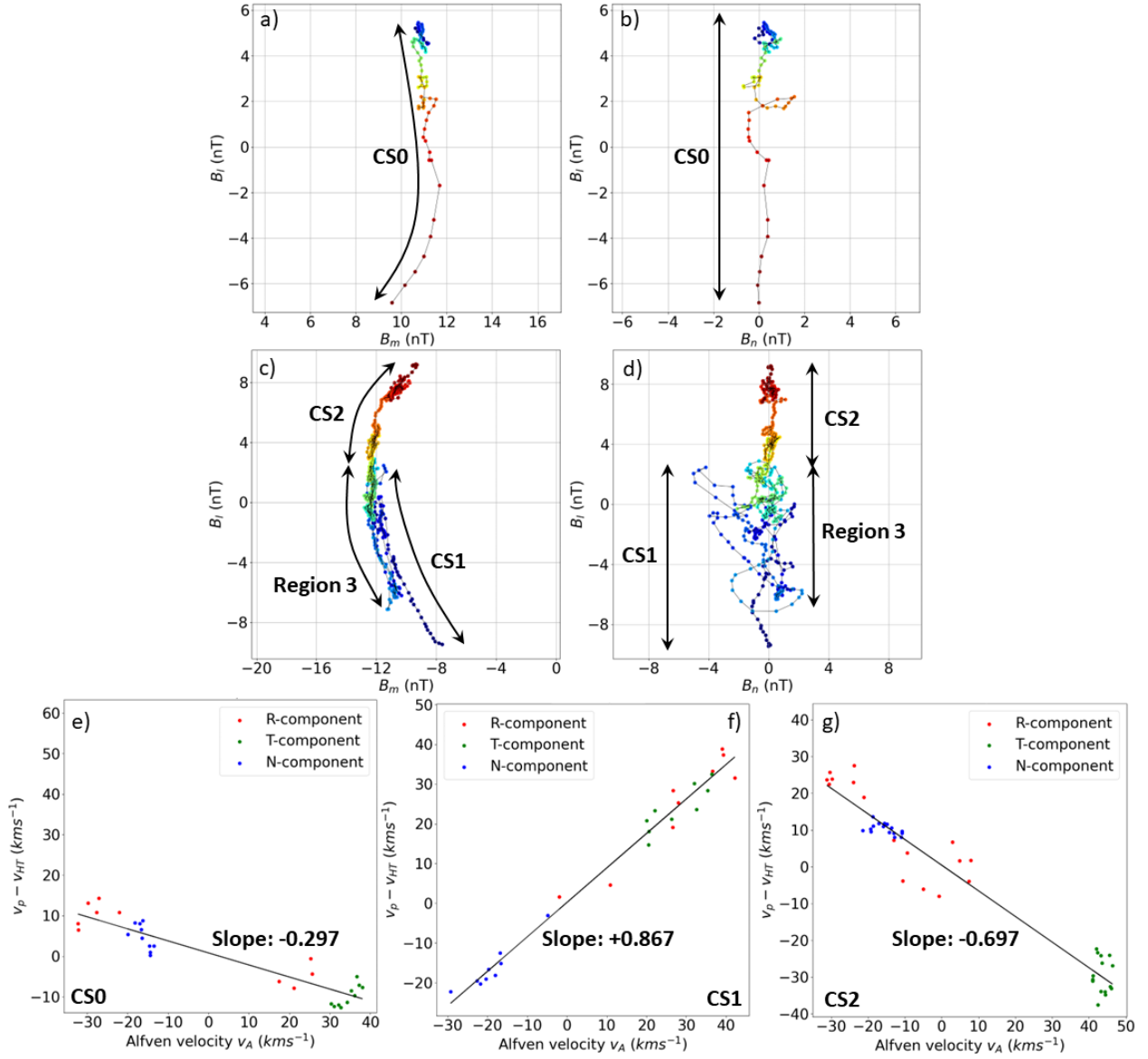


Fig. 6. Magnetic hodographs and Walén plots for CS0 (10:03:35 – 10:03:46 UT), CS1 (10:11:05 – 10:11:10 UT), and CS2 (10:11:41 – 10:12:15 UT) in Event 3. The figure layout is the same as in Figure 2.

$|\mathbf{B}|$ is roughly constant at 12 nT throughout most of Region 2 and is similar in magnitude to $|\mathbf{B}|$ in the background HMF. There is an increase in $|\mathbf{B}|$ between 10:05:20 and 10:05:55 UT that coincides with near-zero B_l and a large deflection in B_n , suggesting that this event contains some internal substructure that is not evident in the other two events. There is no significant change in v_l or $|\mathbf{v}_p^*|$ in Region 2. T_p for the full duration of Region 2 is roughly constant at 13 eV, while n_p increases gradually from 25.5 cm^{-3} to 30 cm^{-3} .

Across CS1 (10:11:05 – 10:11:10 UT), B_l increases from -10 nT to -2 nT and then reverses from -1 nT to +9 nT across CS2 (10:11:41 – 10:12:15 UT). In contrast to Events 1 and 2, the magnetic field does not dwell at a constant orientation in Region 3 (10:11:10 – 10:11:41 UT), but instead shows large fluctuations. The total magnetic shear across these two current sheets is 95° . v_l increases from -15 km s^{-1} to $+20 \text{ km s}^{-1}$, accompanied by a smaller increase in $|\mathbf{v}_p^*|$ from 10 km s^{-1} to 24 km s^{-1} . The peak $|\mathbf{v}_p^*|$ of 35 km s^{-1} is observed in Region 3 and is roughly 75% of the average local $v_A \sim 46 \text{ km s}^{-1}$ in this region. We observe a

small increase in T_p from 14 eV to 17 eV, whereas n_p decreases from a maximum of 30 cm^{-3} to 24 cm^{-3} .

Figure 6 shows the hodographs and Walén plots for Event 3. Although not as distinct as Event 1, we still see an arc in the lm -plane hodographs and a quasi-vertical line in the ln -plane hodographs for all three current sheets. Across CS1 and CS2, the rotation in \mathbf{B} is no longer clearly separated by a dwell period during which the field orientation remains roughly constant. This is caused by the magnetic field fluctuations in Region 3 causing \mathbf{B} to 'double back' on itself in both hodographs. According to the ln -plane hodograph, \mathbf{B} has a smaller B_n -component of -0.1 nT than Events 1 and 2. The Walén plot gradient of -0.297 for CS0 is below the range expected for an Alfvénic RD, whereas the gradients of $+0.867$ for CS1 and -0.697 for CS2 indicates that Alfvénic RDs are present across these two current sheets.

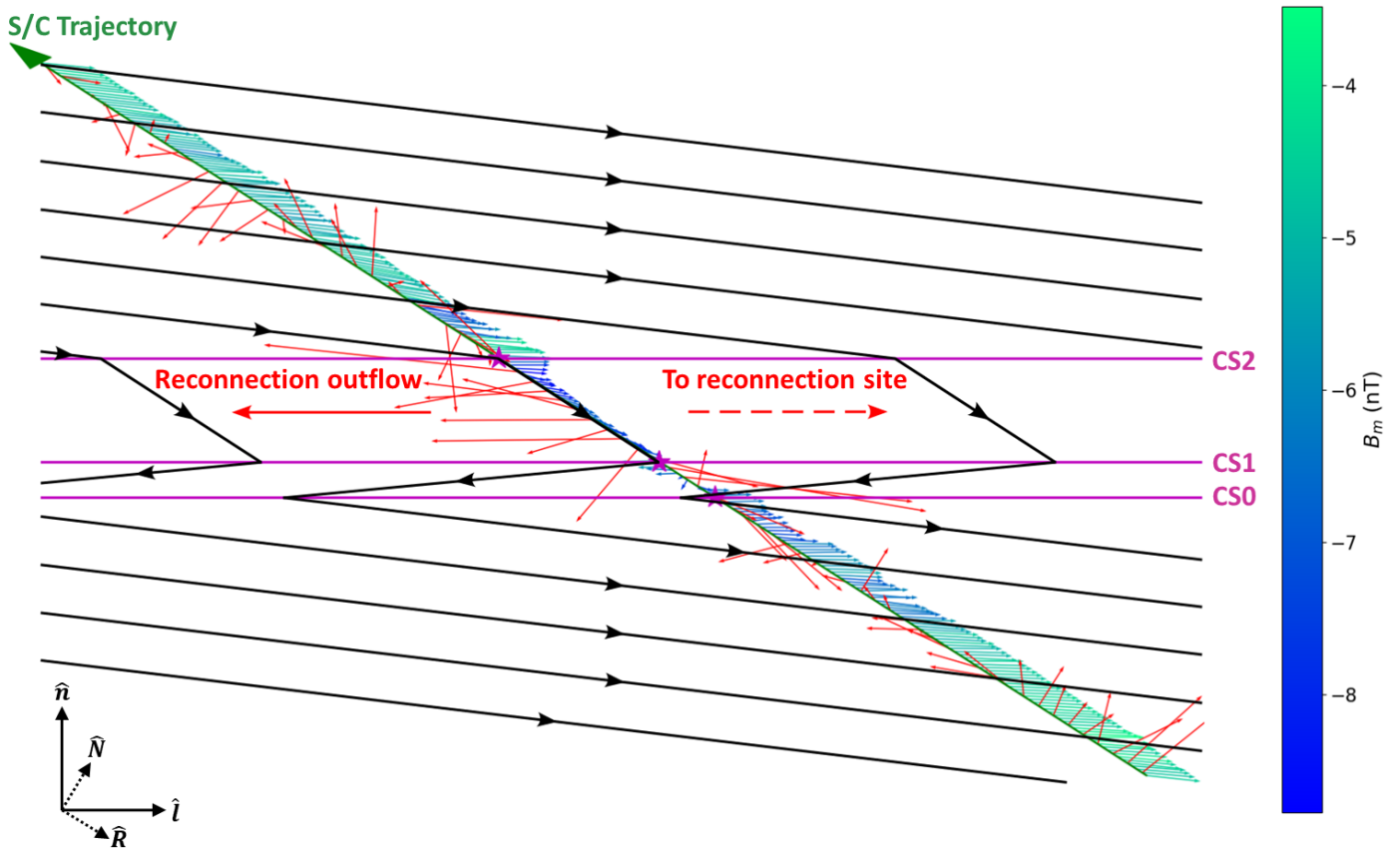


Fig. 7. Feather plot of the \mathbf{B} (blue/light green) and \mathbf{v}_p^* vectors measured in Event 1 in the ln -plane with the spacecraft trajectory marked by the dark green arrow. The B_m component of \mathbf{B} is represented by the colour bar on the right. Overlaid on top is a possible interpretation of the magnetic field configuration of the switchback, shown here by the black arrows. The purple lines mark the assumed configuration of the current sheets CS0, CS1, and CS2. The purple stars show the locations where *Solar Orbiter* crosses the current sheets.

4. Discussion

4.1. Evidence for reconnection at switchback boundaries

Our overall findings suggest that the three observed events are magnetic switchbacks undergoing magnetic reconnection at their trailing edge boundaries. Based on the magnetic field observed in all three events, there is a polarity reversal in B_R , first at CS0 in each case and returning across CS1 and CS2 combined, consistent with magnetic switchbacks. For Event 1, we note the electron strahl PAD data supports this interpretation. As expected, the strahl pitch angle remains constant at 0° both in the background HMF and in Region 2, the polarity-reversed section of the switchback. For Events 2 and 3, we use v_{ap} to confirm if these events are magnetic switchbacks (Fedorov et al. 2021) as the electron strahl PAD data is unavailable. v_{ap} is positive in Regions 1, 3, and 4, where there are no polarity reversals in B_R . Conversely, v_{ap} is negative in Region 2 for both events; $v_{ap} \sim -10 \text{ km s}^{-1}$ for Event 2 and $v_{ap} \sim -20 \text{ km s}^{-1}$ for Event 3. This is in line with the expectation that $v_{ap} > 0$ in the background solar wind and $v_{ap} < 0$ inside the reversed section of a folded field configuration (Marsch et al. 1982; Reisenfeld et al. 2001).

Anti-correlation between the fluctuations in \mathbf{B} and \mathbf{v}_p^* in CS0 and Region 2 of Event 1 is consistent with an Alfvénic structure. However, the $|\mathbf{v}_p^*|$ enhancement of 27 km s^{-1} inside Region 2 is 68% of the local Alfvén speed of 40 km s^{-1} . This is less than the enhancements observed at switchbacks in the near-Sun solar wind, which are often roughly equivalent to the Alfvén speed

(Horbury et al. 2018; Kasper et al. 2019; Horbury et al. 2020b). Combined with the decrease in $|\mathbf{B}|$, accompanying increase in n_p , and the Walén plot for CS0 (Figure 2e), these properties suggest that this event also has a non-Alfvénic component (Kasper et al. 2019; Krasnoselskikh et al. 2020). We do not observe similar correlations or any obvious change in \mathbf{v}_p^* for Events 2 and 3. These velocity enhancements, if they exist, are considerably less than the local Alfvén speed. This property is also noted in reference to previously observed examples of reconnecting switchbacks (Froment et al. 2021).

The trailing edge boundary of all three switchbacks exhibit large increases in $|\mathbf{v}_p^*|$. The regions of accelerated flow at the trailing edge of the switchbacks are bound by a pair of current sheets CS1 and CS2 in each case, across which the fluctuations in \mathbf{B} and \mathbf{v}_p^* are anti-correlated on one side and correlated on the other. This bifurcation of the RCS at the trailing edge of the switchbacks and the presence of an accelerated outflow jet are consistent with the Gosling reconnection model (Gosling et al. 2005a). By contrast, the leading edge boundary of all three switchbacks show no signatures of current sheet bifurcation, and are instead comprised of a single current sheet CS0. Furthermore, with the exception of Event 1, no accelerated flows are observed across CS0 for the three events. This suggests that in each case, reconnection occurs only at the trailing edge boundary of the switchbacks, while the leading edge boundary of the switchback is non-reconnecting.

In the case of Event 1 (Figure 1), the \mathbf{v}_p^* enhancement in the polarity-reversed section of the switchback (Region 2) is oriented in the $+\hat{\mathbf{i}}$ direction, whereas the \mathbf{v}_p^* enhancement in the

trailing edge boundary reconnection outflow region (Region 3) is oriented in the $-\hat{\mathbf{I}}$ direction, suggesting that these two features are distinct from each other. The cause of the strahl dropout and broadening of the strahl PAD across CS1 is unknown but is not an instrumental effect, as a drop in the raw electron counts was also clearly detected by SWA-EAS at this time.

The hodographs show that five out of the six RCS have clear signatures associated with RDs, but the magnitudes of the line of best fit gradients for half of the Walén plots fall below the 0.5–1 range expected for an Alfvénic structure. This suggests that the reconnection outflow is sub-Alfvénic, a result that is not uncommon for reconnection in astrophysical plasmas (Haggerty et al. 2018). Modifying the Walén relation (Equation 3) by factoring in a pressure anisotropy term (Paschmann & Sonnerup 2008) makes no appreciable difference to the results of our analysis. Other reconnection models (Petschek 1964) and observational studies (He et al. 2018; Phan et al. 2020) suggest that the reconnection outflow region boundaries can be composed of a combination of Alfvénic RDs and slow mode shocks. Shocks are not accounted for in the Walén relation (Equation 3) and may reduce the outflow velocity to sub-Alfvénic speeds (Teh et al. 2009; Feng et al. 2017). These may reduce the observed \mathbf{v}_p^* to 34–64% of the predicted v_A (Phan et al. 2013, 2020), which is more consistent with our Walén plots. However, a detailed analysis of different reconnection models lies beyond the scope of our work.

4.2. Switchback and Reconnection Geometry

Figure 7 shows a feather plot of the magnetic field and proton velocity measurements recorded during Event 1. The measured \mathbf{B} is shown by the blue/light green arrows and the measured \mathbf{v}_p^* is shown by the solid red arrows. The colours of the \mathbf{B} arrows represent the strength of the B_m component of the magnetic field. We overlay a possible and consistent interpretation of the magnetic field configuration of the switchback on top, shown by the solid black arrows. As we are limited to measurements along the trajectory of *Solar Orbiter* through this structure, the configuration shown here is one of many possible configurations that we consider consistent with the measurements. We assume that on large scales, the switchback is rigidly frozen into the bulk solar wind flow as it is convected across the spacecraft with constant velocity $\langle \mathbf{v}_p \rangle = (322.2, -5.6, -5.6)_{RTN} \text{ km s}^{-1}$. Under this assumption, we map the measurement time stamps t to spatial coordinates $\mathbf{r} = -(t - t_0)\langle \mathbf{v}_p \rangle$ where t_0 is an arbitrary reference time, defined here at 07:40:00 UT.

The dark green arrow represents the trajectory of *Solar Orbiter* through Event 1, from the bottom right to the top left of the figure. We mark the locations where *Solar Orbiter* crosses CS0, CS1, and CS2 with purple stars. In this assumed configuration, the spacecraft starts in the region of quiet anti-sunward (+R) HMF immediately preceding the switchback. As the spacecraft crosses the leading edge boundary of the switchback (CS0), the polarity of the HMF reverses towards a sunward orientation and $|\mathbf{B}|$ decreases relative to the ambient HMF. \mathbf{v}_p^* gradually increases and is directed in the $+\hat{\mathbf{I}}$ direction.

The trailing edge boundary of the switchback, formed by the current sheets CS1 and CS2, together form a Gosling-type bifurcated RCS (Gosling et al. 2005a) that bounds the reconnection outflow region. In order for the reconnection geometry to be consistent with the observed outflow, we require that the RCS extends back along the solid purple lines towards a reconnection site located off-page, in the $+\hat{\mathbf{I}}$ direction of the spacecraft tra-

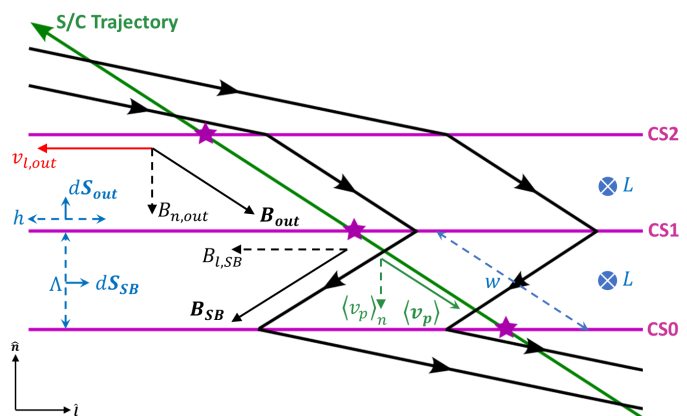


Fig. 8. Simplified diagram of the switchback and reconnection geometry in Event 1, with quantities relevant to the calculation of τ .

jectory. Inside the outflow region, \mathbf{B} is roughly parallel with the spacecraft trajectory. Unlike at the leading edge of the switchback, \mathbf{v}_p^* is directed in the $-l$ direction in this region. After crossing CS2, *Solar Orbiter* exits the switchback and re-enters the surrounding solar wind, where conditions are similar to those observed immediately before the switchback encounter.

In the proposed scenario, magnetic reconnection occurs between oppositely directed field lines at the trailing edge boundary of the switchback. Within the overall geometry of the switchback, this topology may result in the formation of a magnetic flux rope on one side of the reconnection site and kinked magnetic field lines on the other. The strahl PAD in the outflow region (Region 3) shows that *Solar Orbiter* passes through the side of the reconnection site containing open magnetic flux. Magnetic tension in these newly reconnected field causes them to recoil away from the reconnection site and straighten out, unwinding the switchback in the process. In this regard, our interpretation has many similarities with one proposed by Fedorov et al. (2021) to explain the formation of magnetic flux ropes at switchback-like structures observed near 1 au.

4.3. Estimating the timescales for switchback erosion

We can estimate the remaining lifetime, τ , of the three switchbacks discussed in this paper as they are being eroded by magnetic reconnection, assuming reconnection is the sole erosion mechanism and proceeds uniformly at the observed rate. This parameter depends on the magnetic flux ϕ_{SB} remaining in the polarity-reversed portion of the switchback which is yet to be reconnected, as well as the total rate of magnetic flux transport $2\dot{\phi}_{in}$ into the reconnection site from both sides of the reconnection region. As illustrated in Figure 7, our proposed switchback geometry suggests that we only have direct measurements of the magnetic field and plasma in the outflow on one side of the reconnection region. These measurements allow us to quantify the rate of magnetic flux transport, $\dot{\phi}_{out}$, on that side of the outflow. Under the conservation of magnetic flux, $2\dot{\phi}_{in} = 2\dot{\phi}_{out}$, this leads to:

$$\tau = \frac{\phi_{SB}}{\dot{\phi}_{in}} = \frac{\phi_{SB}}{\dot{\phi}_{out}}. \quad (4)$$

Figure 8 shows a simplified diagram of the assumed switchback and reconnection geometry depicted in Figure 7. We first consider the amount of magnetic flux ϕ_{out} transported by the reconnection outflow \mathbf{v}_{out} in time dt . The general expression for

Table 4. Λ : switchback width, B_{SB} : magnetic field strength in the switchback, B_{out} : magnetic field strength in the outflow region, v_{out} : exhaust outflow bulk speed, $\langle v_{SW} \rangle$: average solar wind speed, τ : remaining lifetime of the switchback, D : convection distance travelled by switchback before fully eroding away.

Event	Λ (km)	$B_{l,SB}$ (nT)	$B_{n,out}$ (nT)	$v_{l,out}$ (km s ⁻¹)	$ \langle \mathbf{v}_p \rangle $ (km s ⁻¹)	τ (min)	D (au)
Event 1	3570	-4.8	-1.0	-7.2	322	40	0.005
Event 2	10100	-9.7	0.5	-28.3	439	126	0.02
Event 3	31700	-7.5	-0.1	15.4	443	2005	0.4

magnetic flux through a surface composed of infinitesimal surface elements $d\mathbf{S}$ is given by $\phi = \int \mathbf{B} \cdot d\mathbf{S}$. In this 2D configuration, we define the surface element as $d\mathbf{S}_{out} = hL\hat{\mathbf{l}}$, where $h = v_{l,out}dt$ is the distance the reconnected field lines are connected by the outflow in time t , and L is the out-of-plane extent of the switchback. Hence,

$$\phi_{out} = \int \mathbf{B}_{out} \cdot d\mathbf{S}_{out} \approx B_{n,out}v_{l,out}Ldt, \quad (5)$$

where $B_{n,out}$ is the average B_n -component of the magnetic field in the outflow region. This is equivalent to

$$\dot{\phi}_{out} \approx B_{n,out}v_{l,out}L. \quad (6)$$

The distance w travelled by *Solar Orbiter* in the polarity-reversed section of the switchback (Region 2) is trajectory-dependent and hence, is an unreliable measure for the switchback width. We instead use $\Lambda = \langle \mathbf{v}_p \rangle_n dt_{SB}$, the perpendicular distance between CS0 and CS1, to estimate the width of the polarity-reversed section of the switchback. Here, dt_{SB} is the crossing duration of Region 2. Applying similar reasoning to the derivation of ϕ_{out} above, we estimate the ϕ_{SB} to be:

$$\phi_{SB} = \int \mathbf{B}_{SB} \cdot d\mathbf{S}_{SB} \approx B_{l,SB}\Lambda L. \quad (7)$$

Here, we have oriented the surface element $d\mathbf{S}_{SB} = \Lambda L \hat{\mathbf{l}}$ along the l -direction, as $B_{l,SB}$ is the component of \mathbf{B}_{SB} that reconnects. Finally, we substitute Equation 6 and 7 into Equation 4 to obtain the time remaining until complete erosion of the switchback:

$$\tau = \frac{B_{l,SB}\Lambda}{B_{n,out}v_{l,out}} \quad (8)$$

We estimate the remaining convection distance D until the complete erosion of the switchback as $D \approx |\langle \mathbf{v}_p \rangle| \tau$.

Table 4 shows the estimated τ and D for the three events discussed in this paper. From Equation 8, τ depends linearly on switchback width Λ , which determines the amount of magnetic flux remaining in the polarity-reversed section of the switchback; and is inversely proportional to $v_{l,out}$, which indicates the rate at which reconnected flux is transported away from the reconnection site. Since Event 1 has the smallest width of $\Lambda = 3570$ km and the largest absolute $B_{n,out}$ of 1.0 nT, it has the shortest τ of 40 minutes despite having the slowest absolute $v_{l,out}$ of 7.2 km s⁻¹. Given the small Λ and short τ compared to the other two events, this suggests that Event 1 may be a switchback that has almost been completely eroded by reconnection. Conversely, Event 3 is the widest with $\Lambda = 31700$ km and the smallest $B_{n,out}$ of 0.1 nT, a factor of ten smaller than $B_{n,out}$ for Event 1. As a result, it has the longest $\tau = 2005$ minutes out of the three events. Event 2 is roughly three times wider than Event 1 with $\Lambda = 10100$ km and has $B_{l,SB} = 9.7$ nT twice as large as Event 1, but has the greatest $v_{l,out} = 28.3$ km s⁻¹. Its $\tau = 126$ minutes is thrice as long as for Event 1. D travelled by these three switchbacks before they fully erode range from 0.005 au (Event 1) to 0.4 au (Event 3).

4.4. Implications on switchback formation and evolution in the heliosphere

A key assumption we have made in our calculations in Section 4.3 is that reconnection proceeds uniformly at the observed rate. Because we have no information about the time history of these switchbacks as they evolve from their place of origin to their place of detection, we do not know when or where the onset of reconnection occurs. Therefore, neither τ nor D should be taken as the actual time or distance between reconnection onset and complete erosion of the switchback.

However, τ and D are both small compared to the characteristic timescales and distances of the solar wind expansion, which suggests that reconnection is a fast and efficient mechanism through which switchbacks can be eroded. To highlight this point, let us assume that the onset of reconnection occurs at heliocentric distances similar to PSP perihelion 1 (~ 0.2 au), during which PSP made its observations of prominent switchbacks and switchback patches (Bale et al. 2019; Kasper et al. 2019; Horbury et al. 2020b). If the reconnection rate remains constant during transport in the solar wind, Λ for the observed switchbacks at these distances would be 0.1 – 0.5 solar radii. This is significantly larger than what was observed D by PSP and has two possible implications.

The first is that the switchbacks are formed near the Sun and propagate stably into interplanetary space, before encountering conditions enabling the onset of reconnection and thus the rapid erosion of the switchback. This scenario would explain the rarity of observations of reconnection at switchback boundaries, as the observing spacecraft would need to serendipitously encounter the switchback at almost the same time as reconnection onset. It would also explain why fewer switchbacks are observed at 0.6 – 0.7 au by *Solar Orbiter* compared to PSP at heliocentric distances < 0.2 au. Furthermore, Tenerani et al. (2020) demonstrate that large switchbacks formed in the corona can only survive out to ~ 0.2 au if the background solar wind conditions are sufficiently calm, before the parametric decay instability causes them to decay.

The second explanation is that the switchbacks are formed in-situ in the solar wind at a time much closer to the time of their detection. This is supported by new results from Macneil et al. (2020) and Pecora et al. (2022) that suggest the occurrence rate of magnetic switchbacks increases with heliocentric distance. There is the possibility that two (or more) populations of switchbacks exist: those that form in the Sun's corona, and those that form in the solar wind (Tenerani et al. 2021).

5. Conclusions

Using *Solar Orbiter* data from 10 August and 30 August 2021, we identify three magnetic switchbacks at heliocentric distances between 0.6 – 0.7 au. The trailing edge boundaries of all three events show signatures of jetting and current sheet bifurcation consistent with the Gosling reconnection model (Gosling et al. 2005a).

We propose a possible configuration of the switchback observed on 10 August and reconnection geometry based on measurements of the switchback. In this scenario, reconnection at the trailing edge boundary of the switchback results in the formation of a magnetic flux rope on one side of the reconnection site and kinked field lines on the other. Magnetic tension causes the reconnected field lines to recoil away from the reconnection site, resulting in the unwinding of the switchback. In this paper, we only find cases in which magnetic reconnection occurs at the trailing edge boundary of switchbacks. However, in principle, this process may also occur at the leading edge boundary of switchbacks or at the leading and trailing edge boundaries simultaneously. Although magnetic tension acts naturally to straighten field line kinks in non-reconnecting switchbacks as well, our observation-driven scenario suggests that reconnection can increase the rate at which these structures unwind.

Our estimates of the remaining lifetime of the switchbacks suggest that they erode within a few minutes to a few hours after being observed by *Solar Orbiter*. During this time, the switchbacks are carried a further 0.005 – 0.4 au by the surrounding solar wind flow. If typical, these results could explain why switchbacks are rarely seen at 1 au and has implications on how these structures form and evolve in the heliosphere. The short τ and small D relative to the characteristic timescales and distances of the solar wind expansion show that reconnection is an efficient process for switchback erosion. This suggests that the onset of reconnection must occur during transport in the solar wind in our examples and supports theories of switchback formation in-situ in the solar wind.

There are some caveats to our results and interpretation. The use of single-spacecraft measurements limits our knowledge of the magnetic field and solar wind conditions inside the switchback to what is observed along the spacecraft's trajectory. Furthermore, we also have no information about the time history of the switchbacks. Consequently, we do not know when the onset of reconnection occurs at the switchback boundaries, nor whether this process creates a flux rope embedded within the switchback. Therefore, our interpretation must be understood as one possible scenario that we consider with the measured knowledge of the field and plasma geometry.

In order to further develop the ideas presented here, multi-spacecraft observations will be needed. Radial line-up opportunities between *Solar Orbiter* and other spacecraft such as PSP will allow us to track the temporal evolution of individual switchbacks with heliocentric distance, and identify the conditions required for reconnection to occur at their boundaries. Repeating our analysis on PSP events (Froment et al. 2021) and comparing the results with the ones discussed here would also be an interesting idea to explore in future studies.

Our model predicts that reconnection will convert a portion of the switchback into a magnetic flux rope disconnected from the Sun. Such a structure will appear as a reversal in the HMF polarity but can be distinguished from a switchback in the strahl PAD data. Simultaneous multi-point measurements of the switchback, reconnection outflow region, and flux rope by constellation-type missions such as *Cluster* (Escoubet et al. 1997), *MMS* (Burch et al. 2016), and the upcoming *HelioSwarm* (Klein et al. 2019; Broeren et al. 2021; Matthaeus et al. 2022) will allow us to verify the validity of our model. These types of measurements can also better constrain the 3D geometry of these structures and isolate spatial variations from temporal variations.

Acknowledgements. *Solar Orbiter* is a space mission of international collaboration between ESA and NASA, operated by ESA. *Solar Orbiter* Solar Wind Analyser (SWA) data are derived from scientific sensors which have been de-

signed and created, and are operated under funding provided in numerous contracts from the UK Space Agency (UKSA), the UK Science and Technology Facilities Council (STFC), the Agenzia Spaziale Italiana (ASI), the Centre National d'Etudes Spatiales (CNES, France), the Centre National de la Recherche Scientifique (CNRS, France), the Czech contribution to the ESA PRODEX programme and NASA. Solar Orbiter SWA work at UCL/MSSL was funded by the UK Space Agency under STFC grants ST/T001356/1, ST/S000240/1, ST/X002152/1, ST/W001004/1 and ST/P003826/1. The Solar Orbiter magnetometer was funded by the UK Space Agency (grant ST/X002098/1). T.S.H is supported by STFC grant ST/S000364/1. The author would also like to thank the anonymous referee for their detailed and constructive feedback on an earlier version of the manuscript. For the purpose of open access, the author has applied a Creative Commons Attribution (CC BY) licence to any Author Accepted Manuscript version arising.

References

- Adhikari, L., Khabarova, O., Zank, G. P., & Zhao, L.-L. 2019, *ApJ*, 873, 72
- Bale, S. D., Badman, S. T., Bonnell, J. W., et al. 2019, *Nature*, 576, 237
- Balogh, A., Forsyth, R. J., Lucek, E. A., Horbury, T. S., & Smith, E. J. 1999, *Geophys. Res. Lett.*, 26, 631
- Broeren, T., Klein, K. G., TenBerge, J. M., et al. 2021, *Frontiers in Astronomy and Space Sciences*, 8, 144
- Burch, J. L., Moore, T. E., Torbert, R. B., & Giles, B. L. 2016, *Space Sci. Rev.*, 199, 5
- Cassak, P. A. 2016, *Space Weather*, 14, 186
- de Hoffmann, F. & Teller, E. 1950, *Physical Review*, 80, 692
- De Marco, R., Bruno, R., Jagarlamudi, V. K., et al. 2023, *A&A*, 669, A108
- de Pablos, D., Samanta, T., Badman, S. T., et al. 2022, *Sol. Phys.*, 297, 90
- Dong, X.-C., Dunlop, M. W., Trattner, K. J., et al. 2017, *Geophys. Res. Lett.*, 44, 5951
- Drake, J. F., Agapitov, O., Swisdak, M., et al. 2021, *A&A*, 650, A2
- Drake, J. F., Cassak, P. A., Shay, M. A., Swisdak, M., & Quataert, E. 2009, *ApJ*, 700, L16
- Dudok de Wit, T., Krasnoselskikh, V. V., Bale, S. D., et al. 2020, *ApJS*, 246, 39
- Enzl, J., Přeč, L., Šafránková, J., & Němeček, Z. 2014, *ApJ*, 796, 21
- Escoubet, C. P., Schmidt, R., & Goldstein, M. L. 1997, *Space Sci. Rev.*, 79, 11
- Fargette, N., Lavraud, B., Rouillard, A. P., et al. 2021, *ApJ*, 919, 96
- Fedorov, A., Louarn, P., Owen, C. J., et al. 2021, *A&A*, 656, A40
- Feldman, W. C., Asbridge, J. R., Bame, S. J., Montgomery, M. D., & Gary, S. P. 1975, *J. Geophys. Res.*, 80, 4181
- Feng, H., Li, Q., Wang, J., & Zhao, G. 2017, *Sol. Phys.*, 292, 53
- Fisk, L. A. & Kasper, J. C. 2020, *ApJ*, 894, L4
- Froment, C., Krasnoselskikh, V., Dudok de Wit, T., et al. 2021, *A&A*, 650, A5
- Gosling, J. T. 2012, *Space Sci. Rev.*, 172, 187
- Gosling, J. T., Eriksson, S., & Schwenn, R. 2006a, *Journal of Geophysical Research (Space Physics)*, 111, A10102
- Gosling, J. T., McComas, D. J., Skoug, R. M., & Smith, C. W. 2006b, *Geophys. Res. Lett.*, 33, L17102
- Gosling, J. T. & Phan, T. D. 2013, *ApJ*, 763, L39
- Gosling, J. T., Phan, T. D., Lin, R. P., & Szabo, A. 2007, *Geophys. Res. Lett.*, 34, L15110
- Gosling, J. T., Skoug, R. M., McComas, D. J., & Smith, C. W. 2005a, *J. Geophys. Res. Space Physics*, 110
- Gosling, J. T., Skoug, R. M., McComas, D. J., & Smith, C. W. 2005b, *Geophys. Res. Lett.*, 32, L05105
- Haggerty, C. C., Shay, M. A., Chasapis, A., et al. 2018, *PhPl*, 25, 102120
- He, J., Zhu, X., Chen, Y., et al. 2018, *ApJ*, 856, 148
- Hesse, M. & Cassak, P. A. 2020, *Journal of Geophysical Research (Space Physics)*, 125, e25935
- Horbury, T. S., Matteini, L., & Stansby, D. 2018, *MNRAS*, 478, 1980
- Horbury, T. S., O'Brien, H., Carrasco Blazquez, I., et al. 2020a, *A&A*, 642, A9
- Horbury, T. S., Woolley, T., Laker, R., et al. 2020b, *ApJS*, 246, 45
- Hudson, P. D. 1970, *Planet. Space Sci.*, 18, 1611
- Johnston, Z., Squire, J., Mallet, A., & Meyrand, R. 2022, *Physics of Plasmas*, 29, 072902
- Kasper, J. C., Bale, S. D., Belcher, J. W., et al. 2019, *Nature*, 576, 228
- Khabarova, O., Zank, G. P., Li, G., et al. 2015, *ApJ*, 808, 181
- Khrabrov, A. V. & Sonnerup, B. U. Ö. 1998, *ISSI Scientific Reports Series*, 1, 221
- Kieokaew, R., Lavraud, B., Yang, Y., et al. 2021, *A&A*, 656, A12
- Klein, K. G., Alexandrova, O., Bookbinder, J., et al. 2019, *arXiv e-prints*, arXiv:1903.05740
- Krasnoselskikh, V., Larosa, A., Agapitov, O., et al. 2020, *ApJ*, 893, 93
- Macneil, A. R., Owens, M. J., Wicks, R. T., et al. 2020, *MNRAS*, 494, 3642
- Marsch, E., Rosenbauer, H., Schwenn, R., Muehlhaeuser, K. H., & Neubauer, F. M. 1982, *J. Geophys. Res.*, 87, 35

- Matteini, L., Horbury, T. S., Neugebauer, M., & Goldstein, B. E. 2014, *Geophys. Res. Lett.*, 41, 259
- Matthaeus, W. H., Adhikari, S., Bandyopadhyay, R., et al. 2022, arXiv e-prints, arXiv:2211.12676
- McComas, D. J., Gosling, J. T., Hammond, C. M., et al. 1994, *Geophys. Res. Lett.*, 21, 1751
- Mistry, R., Eastwood, J. P., Phan, T. D., & Hietala, H. 2017, *J. Geophys. Res. Space Physics*, 122, 5895
- Neugebauer, M. & Sterling, A. C. 2021, *ApJ*, 920, L31
- Owen, C. J., Bruno, R., Livi, S., et al. 2020, *A&A*, 642, A16
- Owens, M. J., Crooker, N. U., & Lockwood, M. 2013, *Journal of Geophysical Research (Space Physics)*, 118, 1868
- Owens, M. J. & Forsyth, R. J. 2013, *Living Reviews in Solar Physics*, 10, 5
- Parker, E. N. 1983, *ApJ*, 264, 642
- Parker, E. N. 1988, *ApJ*, 330, 474
- Paschmann, G., Haaland, S., Sonnerup, B. U. Ö., et al. 2005, *Annales Geophysicae*, 23, 1481
- Paschmann, G. & Sonnerup, B. U. O. 2008, *ISSI Scientific Reports Series*, 8, 65
- Pecora, F., Matthaeus, W. H., Primavera, L., et al. 2022, *ApJ*, 929, L10
- Petschek, H. E. 1964, in *NASA Special Publication*, Vol. 50, 425
- Phan, T. D., Bale, S. D., Eastwood, J. P., et al. 2020, *ApJS*, 246, 34
- Phan, T. D., Lavraud, B., Halekas, J. S., et al. 2021, *A&A*, 650, A13
- Phan, T. D., Paschmann, G., Gosling, J. T., et al. 2013, *Geophys. Res. Lett.*, 40, 11
- Pontin, D. I. 2011, *Advances in Space Research*, 47, 1508
- Reisenfeld, D. B., Gary, S. P., Gosling, J. T., et al. 2001, *J. Geophys. Res.*, 106, 5693
- Rosenbauer, H., Schwenn, R., Marsch, E., et al. 1977, *Journal of Geophysics Zeitschrift Geophysik*, 42, 561
- Ruffolo, D., Matthaeus, W. H., Chhiber, R., et al. 2020, *ApJ*, 902, 94
- Schwadron, N. A. & McComas, D. J. 2021, *ApJ*, 909, 95
- Sonnerup, B. U. O. & Cahill, L. J., J. 1967, *J. Geophys. Res.*, 72, 171
- Sonnerup, B. U. Ö. & Scheible, M. 1998, *ISSI Scientific Reports Series*, 1, 185
- Squire, J., Chandran, B. D. G., & Meyrand, R. 2020, 891, L2
- Squire, J., Johnston, Z., Mallet, A., & Meyrand, R. 2022, *Physics of Plasmas*, 29, 112903
- Sterling, A. C. & Moore, R. L. 2020, *ApJ*, 896, L18
- Teh, W. L., Sonnerup, B. U. Ö., Hu, Q., & Farrugia, C. J. 2009, *Annales Geophysicae*, 27, 807
- Telloni, D., Zank, G. P., Stangalini, M., et al. 2022, *ApJ*, 936, L25
- Tenerani, A., Sioulas, N., Matteini, L., et al. 2021, *ApJ*, 919, L31
- Tenerani, A., Velli, M., Matteini, L., et al. 2020, *ApJS*, 246, 32
- Zank, G. P., le Roux, J. A., Webb, G. M., Dosch, A., & Khabarova, O. 2014, *ApJ*, 797, 28